Morphological and Structural Aspects of α-Glucan Particles from Electron Microscopy Observations

Jean-Luc Putaux

Morphological and structural aspects of α-glucan particles from electron microscopy observations

Jean-Luc Putaux

Univ. Grenoble Alpes, CNRS, CERMAV, F-38000 Grenoble, France

jean-luc.putaux@cermav.cnrs.fr

Published in: **Enzymology of Complex Alpha-Glucans**, F. Nitschke ed., CRC Press, 2021, chap. 1, pp. 1–17 - DOI: 10.1201/b22412

1. Introduction

Although similar in terms of chemical composition (they are both homopolymers of α-D-glucose), native glycogen and starch granules lie at opposite ends of the spectrum regarding morphology and structure. Glycogen occurs in the form of water-soluble hyperbranched amorphous nanoparticles, 30-60 nm in diameter [1], whereas native starch granules are several micrometer-large semicrystalline objects, water-insoluble at room temperature, with a fascinating hierarchical and multiscale ultrastructure that has been described in several review articles [2-7]. The variety of shape and size of α(1,4)-linked, α(1,6)-branched polyglucans gets wider if one includes particles in mutants that lack an enzyme involved in the glycogen/starch metabolism [8-11] and those prepared *in vitro*, either by enzymatic biosynthesis [12-14], enzymatic modification of native particles [15], acid hydrolysis of starch granules [16] or *in vitro* recrystallization of α-glucan solutions [17-19].

Specific diffraction and imaging techniques are used to characterize each type of glucan particle at different lengthscales. While X-ray diffraction data provide average information of the crystalline fraction of the specimens [20], high-resolution microscopy techniques such as atomic force [21] or electron microscopy must be used to describe their fine local ultrastructure. In this chapter, we describe practical aspects of sample preparation, contrast enhancing protocols and specific imaging and diffraction techniques to resolve the morphological and ultrastructural characterization of a variety of these glucan particles, using scanning and transmission electron microscopy (SEM and TEM, respectively), in imaging and diffraction modes.

2. Scanning electron microscopy (SEM)

2.1. Principle

A thin focused beam of electrons accelerated at a typical voltage < 30 kV is raster-scanned on the surface of a specimen. The incident electrons make elastic and inelastic collisions with the atoms of the material and different types of electrons are reemitted from the surface and collected with specific detectors. The scanning of the specimen is synchronized with that of a computer screen and the intensity of the signal collected from one point of the surface is used to modulate the intensity of a corresponding pixel on the screen [22]. The scanning speed must be high enough so that the operator only sees one global image due to retinal persistence. SEM micrographs are thus composites images. Their aspect is rather close to that of optical micrographs and their interpretation is often (but not always) intuitive due to the high depth of field and resulting three-dimensional impression. Although only the surface region of the specimen is imaged, a large variety of samples can be observed, from macroscopic objects and fragments of bulk materials to powders of micro- or nanoparticles.

The gun that emits the electrons and the microscope column are designed to focus the incident beam on the surface of the specimen. The recent generation of SEMs is equipped with so-called field emission (FE) guns that produce a very thin and bright beam of highly coherent electrons, which allows reaching a high resolution of about 1 nm. Two main types of re-emitted electrons can be considered. Backscattered electrons are re-emitted upward by the specimen after elastic collisions with the atoms of the material without any significant energy loss. The number of backscattered electrons depends on the average atomic number at the impact point, which thus generates a chemical contrast. Secondary electrons are electrons from the specimen that are ejected after interactions with incident or backscattered electrons. They have a low energy (< 50 eV) and are emitted from a surface layer about 50 nm-thick. Their number mainly depends on the surface topography but also on the average atomic number of the sample. Images produced from secondary electrons show the surface details with a higher resolution [22]. The primary beam can penetrate the specimen to a depth that depends on the accelerating voltage and chemical nature of the material. The volume of interaction is the region of the sample that can produce signals due to interactions with the incident electrons. The effect of the imaging conditions on the "quality" of the resulting SEM micrographs of large α-glucan particles will be discussed in a further section.

Conductive materials can be directly observed by SEM under high vacuum. For non-conductive materials, like many polymers and biological samples, the number of incident electrons can rapidly exceed the number of electrons escaping from the surface, which results in the building of a local charge that may generate artefacts such as image distortions and flash discharges. The first method to cancel such a charging effect is to sputter-coat a thin layer of metal under vacuum on the specimen (typically about 2 nm of gold/palladium alloy) in order to make the surface conductive. In this case, the heavier metal atoms in the surface layer generate more secondary electrons, hence a stronger signal and images with a higher contrast. However, since sputter-coating is performed under high vacuum, hydrated specimens are likely to suffer from the treatment.

The recent generation of SEM instruments offers different possibilities to observe non-conductive samples without resorting to metal-coating. First, for each type of material, there is an optimum voltage at which the number of incident electrons is balanced by the number of electrons escaping the sample. This accelerating voltage is low, typically of the order of 1-2 kV, and sensitive detectors have been developed to collect the weak signals that are emitted at such low voltages. In addition, systems have been specifically designed to keep the specimen under a low pressure of gas (a few tens of Pa) during its observation. These "variable pressure" microscopes can be operated under high or low vacuum conditions since the specimen chamber is separated from the upper high-vacuum column by a differential pumping system.

The benefit is significant in the case of non-conductive materials since the positive ions resulting from the ionization of the residual gas by the emitted electrons somewhat compensate the charging of the specimen [22].

In so-called "environmental" SEMs (or ESEMs), the sample can be observed in a humid atmosphere maintained via a precise control of the temperature and pressure. In order to keep a significant degree of moisture under a low pressure, the temperature must be kept between 3 and 5 °C and the pressure between a few tens and a few hundred Pa. It is even possible to keep liquid water during the observation. Consequently, with an ESEM, plant material [23] or fragments of freshly cut specimens can be observed without resorting first to dehydration by solvent exchange or critical point drying and subsequent metal-coating [24].

Although this chapter is mainly dedicated to the imaging capabilities of electron microscopes, one can briefly mention the possibility to perform chemical analyses in a SEM using so-called energy-dispersive X-ray spectroscopy (EDX). A specific detector collects the X-rays emitted from the specimen surface upon scanning the electron beam and a multichannel analyzer produces corresponding spectra that allow determining the elemental composition [25]. However, the technique has only been used in a very limited number of cases on starch granules. In a context of water purification, the ability of starch granules to absorb chromium ions was studied by mapping and quantifying the distribution of chromium atoms at the surface of and inside the granules [26], whereas chlorine and sulfur atoms were detected in chemically-functionalized starch granules [27]. SEM-EDX may thus be potentially useful to investigate phosphorylation aspects in starch granules.

2.2. SEM observation of starch granules and large glucan particles

Since the average size of native starch granules typically ranges between 1 and 200 µm, SEM is a particularly well-adapted technique to characterize their variety of shapes (**Fig. 1**) [6,28,29]. Specimens can easily be prepared from dry powders or aqueous dilute dispersions deposited onto metallic stubs, cleaved mica or carbon tape, with or without metal coating, as previously explained. Considering the organic nature of starch, backscattered electrons are rarely used to visualize native granules. Most images found in the literature are secondary electron micrographs that allow comparing granules of different botanical origins, from standard to more "exotic" sources [6,30-32], highlighting the peculiarities of some granules like the rodlike or dumbbell shape of *Euphorbiaceae* granules [33,34], or the lateral secondary outgrowth of granules from the *Phajus grandifolius* orchid [35]. Significantly smaller granules purified from leaves, plant chloroplasts, algae or cyanobacteria (typically 1-2 µm) can be observed as well, allowing to identify their three-dimensional shape that otherwise would be more ambiguous when visualized from thin sections of resin-embedded material (see section 2.3.2.3) [36-38].

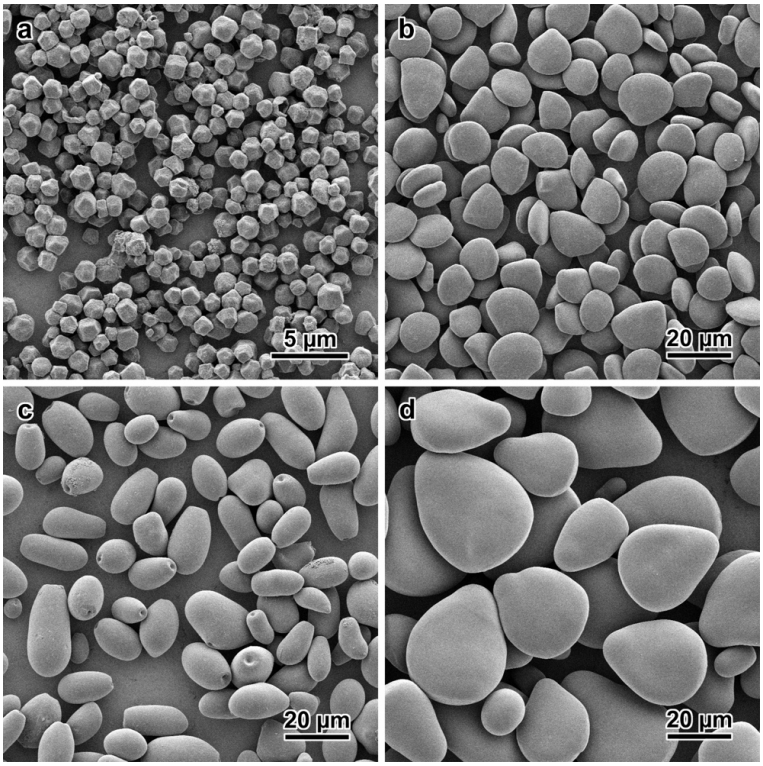

Figure 1. Variety of sizes and shapes of native starch granules of various botanical origins: a) quinoa seeds, b) ginger root, c) avocado nut, d) tulip bulb. Secondary electron FE-SEM images of Au/Pd-coated specimens recorded under high vacuum.

While SEM is mostly used to observe the surface of starch granules [39], the inner structure can be visualized as well, provided that the particles have been fragmented, in particular if they have been submitted to acid hydrolysis or enzymatic digestion that partially etched away some of the material. Such treatments can reveal, for instance, the size and organization of growth rings, or the degradation pattern of acids or amylases [35, 40-44]. Apart from native granules, different types of large starchy particles prepared *in vitro* have been observed as well, such as spherocrystals from heat-treated starch [45,46], debranched starch [47], recrystallized amylose [17], microspheres of retrograded starch [48], B-type axialites of amylose biosynthesized *in vitro* by amylosucrase [12] and A-type single crystals from short-chain amylose [19].

A survey of the SEM micrographs found in the literature shows that the specimens are not necessarily observed under optimal imaging conditions, which may result in missed information or misinterpreted artefacts. In particular, the choice of accelerating voltage is critical. At high voltage (typically 10-30 kV), the incident electrons can penetrate deeper in the organic material, thus generating cascades of collisions in a larger interaction volume that, in turn, generates secondary electrons from a region of the surface laterally much wider than that irradiated by the primary beam [22]. Although the number of emitted electrons is higher and the particles appear brighter, there is an overlap of information in the signals collected from

neighboring points, resulting in a loss of resolution. At a lower acceleration, the volume of the primary beam interaction in the specimen is much smaller and the secondary electrons are emitted from a narrower region. The surface topography is thus revealed in more details.

This influence of accelerating voltage is illustrated by **Fig. 2** that shows FE-SEM micrographs of uncoated waxy maize starch granules observed under high vacuum or low air pressure. Although the contrast of the granules increases with increasing voltage, the high-resolution details on the surface are lost. This "smoothing" effect can be misinterpreted as radiation damage. For this uncoated specimen, the optimum conditions would be close to those corresponding to **Fig. 2b** where the charging is minimal while the contrast is satisfactory and details can still be seen at the granule surface. The effect is even more significant for small granules and particularly flat ones. At high voltage, the electrons can penetrate deeper than the thickness of the granules and partly interact with the supporting material. In **Fig. 3d**, the metal-coated *Arabidopsis* leaf starch granules imaged at 10 kV are very bright but they also look very smooth, while at 1 or 2.5 kV (**Fig. 3a** and **3b**, respectively), the contrast is lower but the high-resolution texture of the granule surface is visible.

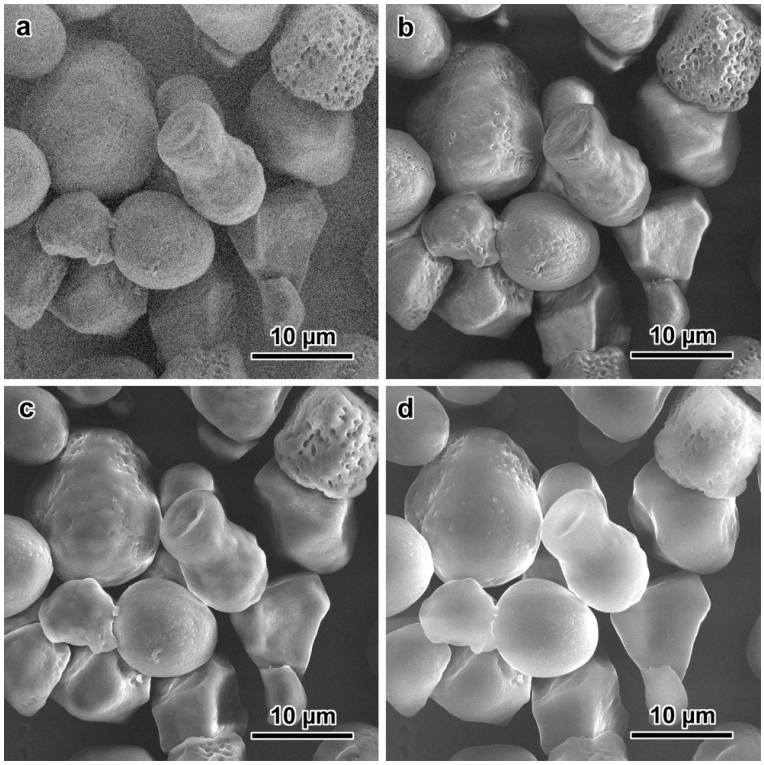

Figure 2. Secondary electron FE-SEM images of uncoated waxy maize starch granules recorded at a magnification of 3000×. The same region of the preparation has been imaged at different accelerating voltages of the electrons and air pressures: a) 2 kV, low pressure of air (40 Pa); b) 4 kV, 40 Pa; c) 10 kV, 70 Pa; d) 20 kV, 70 Pa.

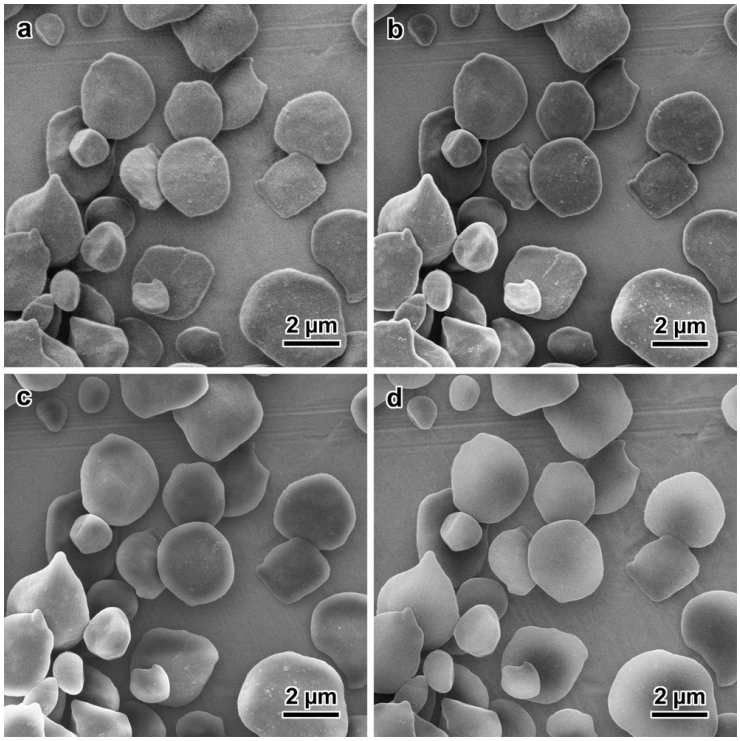

Figure 3. Secondary electron FE-SEM images of Au/Pd-coated flat starch granules from *A. thaliana* leaves (*Wassilewskija* ecotype) recorded under high vacuum at a magnification of 10000×. The same region of the preparation has been imaged at different accelerating voltages: a) 1 kV; b) 2.5 kV; c) 5 kV; d) 10 kV. Sample courtesy of F. Wattebled (UGSF, University of Lille).

As mentioned earlier, ESEM is an attractive technique to directly observe hydrated plant material and, more particularly, starch granules within their tissue environment. As an example, **Fig. 4** shows secondary electron images of a freshly cut fragment of potato tuber that was directly introduced into the microscope chamber without fixative treatment. The fragment was first observed under fully hydrated conditions (**Fig. 4a**), then after controlled partial drying (**Fig. 4b**). In both conditions, the starch granules are seen inside cellulosic cells with a very good contrast, even without metal coating. **Fig. 4c** to **4e** show one starch granule that was alternatively imaged in wet, hydrated and dry conditions by slightly changing the specimen temperature and gas pressure in the chamber. Liquid water droplets can thus be reversibly stabilized during observation or dried, which allows studying the dynamic effects of water sorption or dehydration of starch granules and large glucan particles. However, care must be taken to record images at a relatively low magnification since, under humid conditions, the specimens can be more rapidly damaged under electron illumination due to the enhanced diffusion of the radiation defects. So far, only a few ESEM images of starchy specimens can be found in the literature. In particular, the technique was used to characterize the pores on the surface of starch granules [49], the effect of milling on rice grains [50] and wheat endosperm [51,52], as well as the effect of relative humidity on the volume change in rice powders [53] and starch surfaces [54].

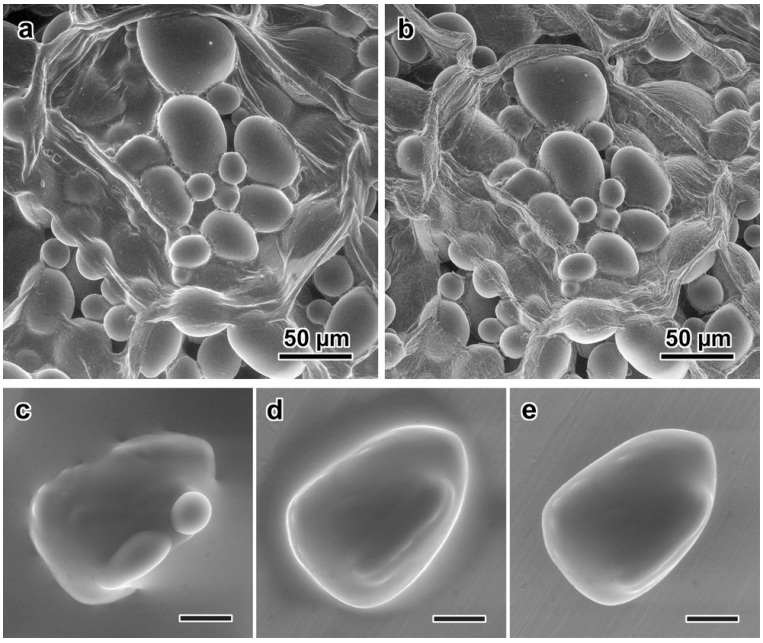

Figure 4. a,b) Secondary electron ESEM images of an uncoated freshly cut fragment of a potato tuber: a) the specimen temperature was 2 °C and the pressure of humid air 700 Pa, maintaining a 99% humidity around the specimen. The accelerating voltage was 10 kV. b) The pressure was decreased to 200 Pa and the humidity was 30%). The accelerating voltage was 5 kV. Note how the cell walls gets more wrinkled and the granules get closer to each other upon drying. c-e) Secondary electron ESEM images of a native starch granule for *Phajus grandifolius* recorded at about 3 °C. From "c" to "e", the pressure of humid air was decreased, resulting in the drying of the granule: c) the granule is soaked and droplets of liquid water can be seen; d) the granule is hydrated with visible traces of humidity; e) the granule is under high vacuum. Scale bar in images "c" to "e": 20 µm.

3. Transmission electron microscopy (TEM)

3.1. Principle

A beam of electrons accelerated at a typical voltage of 100-300 kV is transmitted through a thin specimen (< 500 nm for organic materials) to form a magnified image of its contours and projected volume with a potential resolution of a few ångstroms. Scattering of the electrons by the atoms of the material and the use of selective apertures in the microscope column generate contrasts in the images [25]. Another major advantage of TEM is the possibility to record local electron diffraction patterns of semicrystalline specimens and therefore study the structure and orientation of the crystalline domains. However, organic samples are extremely sensitive to radiation damage from the electron beam. They are rapidly degraded at room temperature and therefore, must be observed under low illumination conditions. Organic specimens can also be preserved for a longer time if they are observed at higher voltage or kept at low temperature during the observation. Hydrated specimens must be quench-frozen before introduction in the microscope to prevent vacuum drying, and observed at low temperature.

3.2. Sample preparation and contrast enhancement techniques

One of the main constraints for TEM observation is that the specimens must be very thin. Glycogen particles, with a typical diameter of a few tens of nanometers, can be readily imaged from dilute aqueous suspensions (typically 0.001-0.01 % w/v, without any buffer salts that would crystallize upon drying). Much larger objects like starch granules, recrystallized spherulites or plant tissues containing glucan particles cannot be observed as such and thin sections must be prepared using ultramicrotomy.

3.2.1. Particle suspensions

3.2.1.1. Grid pretreatment and negative staining

Achieving a satisfying distribution of particles from suspensions on the carbon film with limited aggregation or overlapping can be challenging. This is particularly critical when one wants to determine the size distribution of a population of glycogen particles. The supporting carbon film being initially hydrophobic, the direct deposition of aqueous suspensions and subsequent air-drying generally result in locally accumulated material. The so-called "glow discharge" procedure is efficient to treat carbon films prior to sample deposition [55, 56]. The carbon-coated TEM grids are placed in a chamber in which a low pressure of air is ionized. The grids are submitted to this mild plasma cleaning during a few seconds which results in a temporarily hydrophilic carbon surface onto which aqueous suspensions easily spread. As charges are generated on carbon during the treatment, the particles also tend to adsorb on the surface. The excess of liquid is thus gently blotted away with filter paper and the objects should remain homogenously distributed on the supporting film.

3.2.1.2. TEM observation of negatively stained polyglucan particles

Glycogen has been one of the first biopolymers to be observed in the early age of TEM development. However, the images produced by Husemann and Ruska did not reveal any fine details of the particles [57]. The reasons of this poor contrast are that i) drying induces a shrinking of the macromolecules, ii) the constituting light atoms do not generate any significant scattering contrast, and iii) the particles are prone to rapid degradation under the electron beam. The most widely used technique to enhance the contrast of individual nano-objects is negative staining. Briefly, a drop of an aqueous solution of heavy-atom salt is deposited on the specimen. Upon drying, a thin layer of heavy atoms concentrates around the nanoparticles, creating an electron-dense cast [56]. The particles thus appear as clear objects on a darker background. The preparations can be observed at a higher magnification since, although the glucan particles are indeed damaged by the electron beam, the heavy atom cast is resistant

and thus reveals the contours and fine details of the surface topography. Up to now, the most commonly used stains have been aqueous uranyl acetate (2 % w/v), and phototungstic acid, to a lesser extent. However, due to recent regulations regarding the handling of radioactive compounds, uranyl acetate will soon be replaced by new staining solutions that do not contain uranium [58,59]. Practically, a homogenous negative staining of particles can be achieved under two conditions: i) the supporting carbon film has to be glow-discharged before depositing the nanoparticles and the stain, and ii) the stain solution has to be applied on the specimen before drying. After a few minutes, the stain in excess can be blotted away with a filter paper and the residual thin film of stain allowed to dry.

Examples of TEM images of negatively stained preparations of oyster glycogen and maize phytoglycogen are shown in **Fig. 5a** and **5c**, respectively. Many other images of negatively stained glycogen and phytoglycogen from various sources can be found in the literature: rat and mouse liver [60-63], rat muscle [64], pig liver [65,66], oyster [67,68], slipper limpet [61], and *sugary*-1 maize mutant [66,69,70]. On such images, the smaller spheroidal β-particles can clearly be distinguished from the larger multilobular α-particles that have been described as supramolecular clusters of β-particles [60,61,65]. Size distribution histograms of each population can be determined from the images, even though the larger particles may be deformed due to the flattening induced by drying. These morphological data can be compared to the various mathematical models that describe the hyperbranched architecture of the macromolecule and address the question of a possible limitation in size of native glycogen due to peripheral chain crowding [71-75].

Glycogen-like hyperbranched particles have been synthesized *in vitro* using enzymes, and observed after negative staining. Examples of one-pot biosynthesis consisted in incubating short-chain amylose with the branching enzyme (BE) from the hyperthermophilic bacteria *Aquifex aeolicus* [13,76] or that from *Rhodothermus obamensis* [77]. Branched polyglucans were also synthesized by the tandem reaction of an elongation enzyme, to yield amylose-like chains, and a BE. Successful combinations contained the amylosucrase from *Neisseria polysaccharea* and the BE from *R. obamensis* in the presence of sucrose [78], or phosphorylase *b* from rabbit muscle and the BE from *Deinococcus geothermalis* in the presence of glucose-1-phosphate [14].

Starch granules purified from algae, cyanobacteria, parasites or leave chloroplasts can be observed by TEM after deposition on a carbon film, provided that their thickness does not exceed 500 nm. In many cases, the smaller granules are lenticular with a diameter < 1 µm and a thickness not exceeding 200 nm and details of the surface structure can be revealed by negative staining. A short and mild acid pre-treatment that etches away some of the granule surface material can be helpful [79]. In this line, a lamellar organization has been clearly

revealed in the semi-amylopectin granules of different species of Porphyridiales [80] and in amylopectin granules of *Cryptosporidium parvum* oocysts [81]. Thicker granules can be directly visualized by SEM (section 2.2) or embedded in a hardening resin and their ultrathin sections observed by TEM (section 3.2.3).

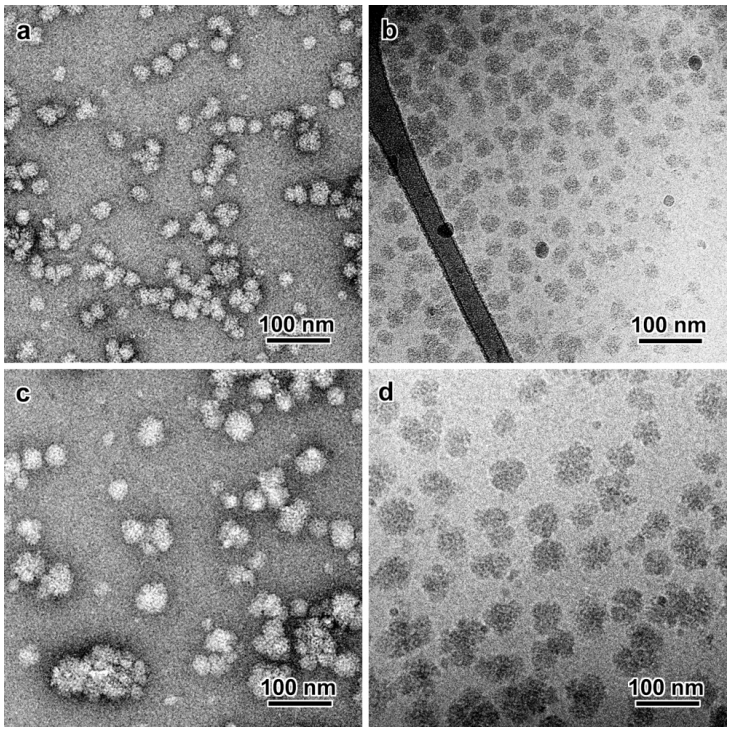

Figure 5. TEM images of glycogen particles from oyster (a,b) and phytoglycogen from the *sugary*-1 maize mutant (c,d). In images "a" and "c", the preparations have been negatively stained with uranyl acetate while in "b" and "d", the particles were unstained, embedded in a thin film of vitreous ice and observed at low temperature by cryo-TEM.

When the starch granules are significantly bigger, a longer treatment in sulfuric acid (Naegeli's method) or hydrochloric acid (so-called "lintnerization" [82]) results in the progressive disruption of the granule architecture. This has been illustrated in the case of waxy maize starch granules hydrolyzed with 2.2 N HCl at 36 °C [16]. After 2 weeks, negatively stained granule fragments exhibited a lamellar organization (**Fig. 6a**) while, after 6 weeks, parallepipedal platelets were individualized, lying flat on the carbon film (**Fig. 6b**). A similar behavior was observed for waxy maize starch granules hydrolyzed with 3.2 M H_2SO_4 at 30 °C 6 during weeks [83] or at 40 °C under constant stirring during one week [84]. These platelet nanoparticles would correspond to the lamellae in the cluster model of amylopectin where the short linear branches form crystalline arrays of parallel double helices [6,82]. It was assumed that the acid preferentially severed the more accessible α(1,6) branching point in the interlamellar regions, thus allowing the crystalline platelets to separate [16[. However, the chromatography analysis of H_2SO_4-hydrolyzed waxy maize starch granules revealed that the nanocrystals also

contained a significant number of branch points [84]. Lintners were prepared from potato [85] and barley [86] starch granules as well, but the shape of the resulting platelets was less defined.

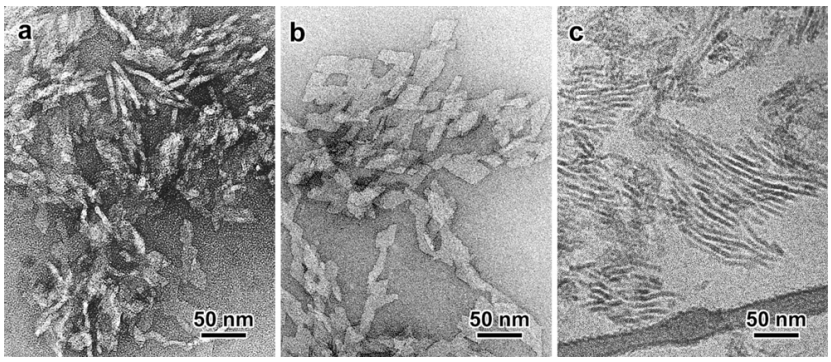

Figure 6. a,b) TEM images of negatively stained nanocrystals prepared by acid hydrolysis of waxy maize starch granules after 2 (a) and 6 (b) weeks of hydrolysis in 2.2 N HCl, at 36 °C. In "a", the clear elongated units are 7-9-nm-thick lamellae seen edge-on while the platelets in "b" would correspond to individual lamellae lying flat on the carbon film. c) Cryo-TEM image of unstained fragments after 2 weeks of hydrolysis. Here, the stacked lamella seen edge-on are dark, partly due to diffraction contrast. Image "a" courtesy of H. Angellier-Coussy (CERMAV, LGP2, Grenoble), printed with permission.

3.2.2. Cryo-transmission electron microscopy (cryo-TEM) of particle suspensions

Cryo-TEM can be used to observe nanoparticles in aqueous suspension when drying or staining is thought to induce artefacts such as deformation, aggregation or crystallization of buffer salts. This technique is particularly helpful for soft or water-swollen colloidal nanoparticles whose morphology or structure would be affected by air-drying or staining. As described in more details elsewhere [56,87], droplets of suspensions are deposited on lacey carbon films supported by TEM grids, or on perforated support foils with calibrated holes. Using dedicated automatized workstations, the liquid in excess is blotted with filter paper and the remaining thin film standing over the support holes is quench-frozen in liquid ethane. The frozen specimen is then mounted in a pre-cooled cryo-specimen holder, introduced into the microscope, and observed at low temperature (around -180 °C).

Examples of cryo-TEM images of oyster glycogen and maize phytoglycogen are shown in **Fig. 5b** and **5d**, respectively. In this case, the concentration of the suspension must be about 100 times higher than for the preparation of dry specimens (typically 0.1 to 1.0 % w/v). The well-dispersed unstained particles are seen embedded in a thin film of transparent vitreous ice. Cryo-TEM is not yet a routine technique compared to negative staining. Although it is perfectly adapted to visualize glucan particles frozen in their water-swollen state, only a few images can be found in the literature. Putaux et al. compared the size distributions of *sugary-1* maize phytoglycogen particles determined from TEM images of negatively stained,

metal-coated and quench-frozen preparations [88]. Martinez-Garcia et al. compared the morphology of glycogen particles from various bacterial sources [89]. Cryo-TEM has also been used to visualize core-shell particles prepared by enzymatic extension of oyster glycogen surface chains by the amylosucrase of *N. polysaccharea* in the presence of sucrose [15], as well as glycogen-like hyperbranched particles synthesized *in vitro* by phosphorylase *b* and a glycogen branching enzyme [14]. As aforementioned, small fragments of starch granules that partially retain the lamellar organization of amylopectin can be prepared by mild acid hydrolysis of the native granules. **Fig. 6c** shows such fragments imaged by cryo-TEM after quench-freezing. In this case, the contrast does not result from any staining but is partly due to the diffraction by the crystalline lamellae.

3.2.3. Ultramicrotomy of bulk samples and large particles

Soft and hydrated materials such as leaf fragments, microalgae or cyanobacteria cannot be directly sectioned. They have to be chemically fixed in paraformaldehyde/glutaraldehyde, post-fixed with osmium tetroxide (OsO_4), dehydrated by exchange with ethanol and embedded in hardening resins [90]. Purified starch granules can be directly soaked in the liquid resin before hardening. Ultrathin (50-150 nm) sections of the embedded specimens are then cut at room temperature with a diamond knife, in an ultramicrotome [91]. The sections float on water and are collected on bare or carbon-coated TEM grids. When the sample is soft at room temperature, ultrasectioning must be performed under cryogenic conditions in a dedicated unit.

Different techniques can be used to enhance the contrast of the organelles or particles in the sample. On the one hand, before the dehydration step, the sample can be treated with uranyl acetate so that it is already stained when it is soaked in the resin. On the other hand, the thin sections can be post-stained with uranyl acetate/lead citrate [91]. In both cases, the glucan particles generally remain unstained and appear as clear objects on a darker background, as illustrated by the image of *Arabidopsis* chloroplasts in **Fig. 7a** and by many of those found in the literature [92-95]. Specific staining techniques have been proposed to selectively stain glycogen particles inside animal tissues [96-98] like, for instance, the addition of potassium hexacyanoferrate ($K_3Fe(CN)_6$) to the classical OsO_4 post-fixative [99]. Another technique of interest to reveal the presence of glucan particles in thin sections has been developed by Gallant et coll. [100]. The sections are treated with periodic acid thiosemicarbazide silver proteinate (PATAg) that positively stains molecules that contain sugar units [101]. Condensed glucan particles thus appear as dark objects: glycogen as small dots and starch granules as more extended regions [102-105]. Note that glycoproteins and glycolipids can be stained as well, thus outlining organelles and cell walls. An example of PATAg-treated *Arabidopsis* leaf plastids is shown in **Fig. 7b**.

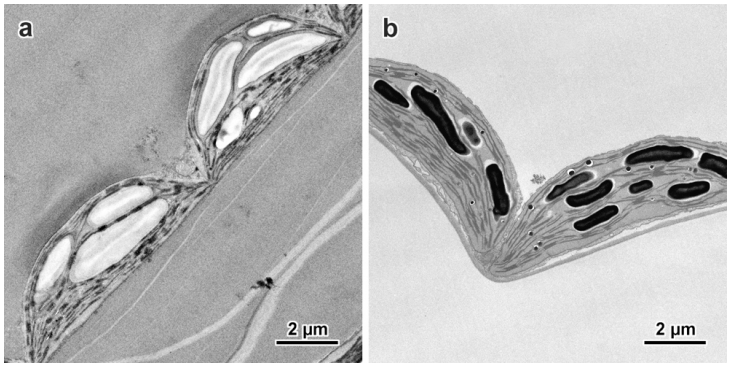

Figure 7. TEM images of ultrathin sections of fragments of resin-embedded wild-type *A. thaliana* leaves: a) chloroplasts from the Columbia ecotype. The sample has been stained "in block" with uranyl acetate before sectioning. The starch granules are not stained and appear as clear elongated regions. b) Chloroplasts from the *Wassilewskija* ecotype. The thin section has been treated with the PATAg method and the positively stained starch granules are dark. Samples courtesy of L. Boyer and F. Wattebled (UGSF, University of Lille).

One artefact sometimes observed on ultrathin sections of resin-embedded starch granules is the presence of dark ripples across the granule sections. This effect, which does not depend on the size of the granules and may occur on 1-2 µm-large plastidial starch as well as 50-100 µm-large tuber granules, has been studied by Gallant and Guilbot. It would be due to an insufficient permeation of the granules by the inclusion agent and also to the partial swelling of the granule sections while they float on water, resulting in local folding of the section [106]. However, images of thin sections without any folding effect, even from large granules, can be found in the literature [107], which suggests that the effect may also depend on the nature of the embedding resin and operating conditions during ultramicrotomy (angle of the diamond knife, sectioning speed, etc.).

It must be noted that the ultramicrotome can also be used to prepare mirror-like surfaces from blocks of resin-embedded material. This surface can then be observed by SEM using backscattered electrons, sensitive to atomic number, to reveal the regions that were specifically stained by OsO_4 and other contrasting agents. However, since most embedding resins are non-conductive, the blocks must be observed under low-vacuum conditions in order to suppress the charging effects (see section 2.2). Even though the resolution of such block face images is lower than those of TEM micrographs of corresponding ultrathin sections, their contrast is high and the field of view is not limited by the bars of the supporting TEM copper grid. This method is thus particularly useful to check the quality of the embedding and staining before actual preparation of ultrathin sections from the same block. **Fig. 8** shows a comparison of the block face SEM image and corresponding TEM micrograph of an ultrathin section of the same region. Block surfaces of resin-embedded starch granules have also been used to record topography images by AFM, reveal details of the granule inner structure [108] and study the deformation artefacts induced by the diamond knife during cutting [109].

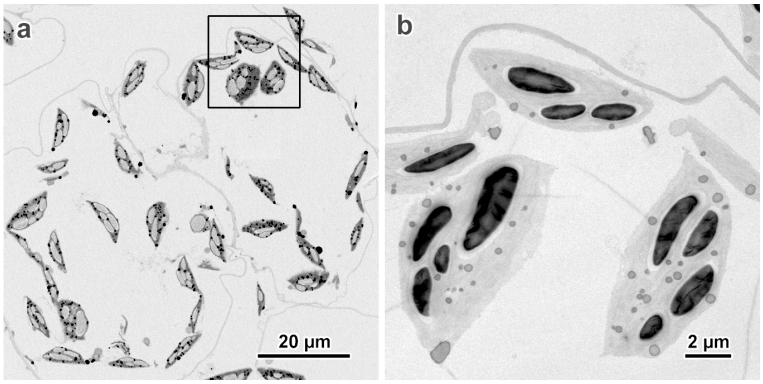

Figure 8. a) Backscattered electron FE-SEM image of chloroplasts in a fragment of *A. thaliana* leaf (Columbia ecotype) embedded in resin. The block has been surfaced with a diamond knife. The contrast of the image has been reversed for clarity. The regions enriched in OsO_4 are dark and the starch granules are unstained. b) TEM image of an ultrathin section of the same block stained by the PATAg method. The starch granules are dark. The image corresponds to the region framed on the SEM image in "a". The starch granule content appears to be different because the section was cut at a slightly different height in the block. Sample courtesy of M. Facon and F. Wattebled (UGSF, University of Lille).

3.2.4. Electron diffraction of crystalline specimens

Thin sections of starch granules can be observed without any staining, provided that the semicrystalline internal structure has not been affected by a fixative treatment and that the embedding resin does not impregnate the granules [83]. Chanzy et al. [110] and Helbert and Chanzy [107] used a water-soluble melamine resin to embed native and acid-hydrolyzed corn starch granules. Since the thin sections prepared by ultramicrotomy did not initially exhibit any contrast, they were briefly submitted to a mild HCl hydrolysis, resulting in the partial etching of the resin and revealing the location of the granules [107]. The growth rings of previously partially lintnerized granules were visible under low-dose illumination (**Fig. 9a**). Electron diffraction patterns were recorded at low temperature under frozen-hydrated conditions, which corresponded to the A-type and confirmed, at the micron scale, the radial orientation of the double helices in the crystalline domains with respect to the growth rings (**Fig. 9a**) [107]. Similar electron fiber diffraction patterns had previously been recorded from frozen-hydrated fragments of B-type potato starch granules [111]. Highly crystalline spherocrystals prepared by crystallization of short-chain amylose from solution could also be sectioned after embedding in melamine resin subsequently cured at room temperature to prevent the partial dissolution of the particles. Well-resolved A-type electron diffraction patterns were recorded at low temperature from quench-frozen hydrated sections, revealing the radial orientation of the amylose double helices (**Fig. 9b**) [17].

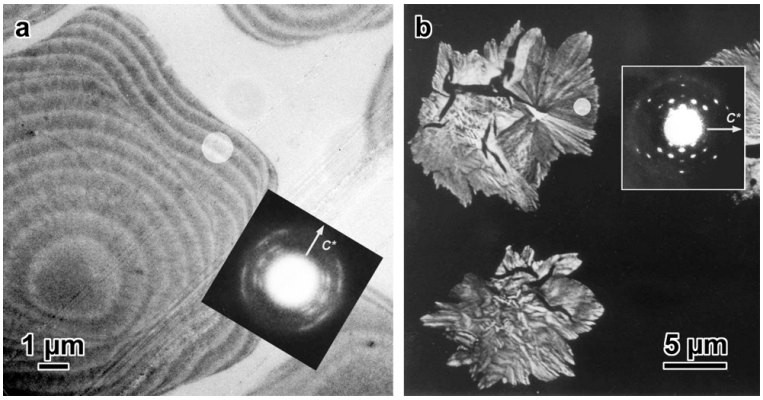

Figure 9. a) Bright-field TEM image of an ultrathin section of partially HCl-hydrolyzed native corn starch granules embedded in melamine resin. No additional staining was used to reveal the growth rings. Inset: electron diffraction fiber pattern recorded from the region of the granule indicated by the clear disk. The pattern shows that the fiber axis *c* is oriented perpendicular to the growth rings. In order to record this pattern, the hydrated section has been quench-frozen in liquid nitrogen prior to introduction in the microscope and observed at low temperature. b) Dark-field TEM image of a frozen-hydrated ultrathin section of A-type amylose spherocrystals embedded in melamine resin. Inset: electron diffraction pattern of the region indicated by the clear disc, showing that the *c*-axis of the crystallites is radially oriented. Images and diffraction patterns courtesy of W. Helbert (CERMAV, Grenoble), printed with permission.

4. Perspectives

As explained earlier, TEM images are 2D projections of the volume of objects along the beam direction. Information along this direction is thus lost. One of the most exciting developments in TEM is the possibility to reconstruct the volume of specimens using series of 2D images recorded at consecutive tilt angles of the specimen. This can be achieved in modern microscopes by taking advantage of highly sensitive digital cameras and software that precisely control the specimen orientation and the image acquisition. After alignment with respect to one another, the collected 2D images are back-projected to calculate a 3D reconstruction of the specimen volume [112,113]. Now widely used to study the morphology and structure of biological systems, this electron tomography approach could be applied to address several questions related to $\alpha(1,4)\alpha(1,6)$ glucan particles. For instance, the ultrastructure of glycogen α-particles could be studied in their water-swollen state by determining the 3D organization of the constituting β-units from series of cryo-TEM images. Visualizing the spatial organization of amylopectin lamellae in very small starch granules like those from chloroplasts [114] would also be particularly useful to shed more light on the much-debated architecture of larger starch granules.

Acknowledgments

Except when explicitly indicated, the micrographs displayed in this article have specifically been recorded for this chapter. The SEM images in **Figs. 1-4** and **8a** have been recorded using a FEI Quanta 250 microscope equipped with a field-emission gun while the TEM micrographs in **Figs. 5-7** and **8b** have been recorded with a FEI-Philips CM200 'Cryo' microscope operating at 80 or 200 kV. The author would like to thank the NanoBio-ICMG Platform (FR 2607) for granting access to the Electron Microscopy facility, Christine Lancelon-Pin (CERMAV, Grenoble) for recording the FE-SEM images, Fabrice Wattebled (UGSF, Lille) for giving a sample of *Arabidopsis* starch granules, and Henri Chanzy (CERMAV) for his critical reading of the manuscript.

References

[1] Manners, D.J. **1991**. Recent developments in our understanding of glycogen structure. *Carbohydr. Polym. 16*, 37–82. https://doi.org/10.1016/0144-8617(91)90071-J

[2] French, D. **1984**. "Starch, Chemistry and Technology", R.L. Whistler, J.N. BeMiller and E.F. Parschall Eds, Academic Press, NewYork, p. 183–247.

[3] Zobel, H.F. **1988**. Molecules to granules: a comprehensive starch review. *Starch/Staerke 40*, 44–55. https://doi.org/10.1002/star.19880400203

[4] Buléon, A., P. Colonna, V. Planchot and S. Ball. **1998**. Starch granules: structure and biosynthesis. *Int. J. Biol. Macromol. 23*, 85–112. https://doi.org/10.1016/S0141-8130(98)00040-3

[5] Tang, H.J., T.H. Mitsunaga and Y. Kawamura. **2006**. Molecular arrangement in blocklets and starch granule architecture. *Carbohydr. Polym. 63*, 555–560. https://doi.org/10.1016/j.carbpol.2005.10.016

[6] Pérez, S. and E. Bertoft. **2010**. The molecular structures of starch components and their contribution to the architecture of starch granules: A comprehensive review. *Starch/Stärke 62*, 389–420. https://doi.org/10.1002/star.201000013

[7] Lourdin, D., J.-L. Putaux, G. Potocki-Véronèse, C. Chevigny, A. Roland-Sabaté and A. Buléon. **2015**. Crystalline structure in starch. In "Starch - Metabolism and Structure". Y. Nakamura ed., Springer Japan, pp. 61–90. https://doi.org/10.1007/978-4-431-55495-0_3-

[8] Woodford, B and M.O.M. Tso. **1980**. An ultrastructural study of the corpora amylacea of the optic nerve head and retina. *Am. J. Ophthalmol. 90*, 492–502. https://doi.org/10.1016/S0002-9394(14)75018-4

[9] Leel-Ôssy, L. **2001**. New data on the ultrastructure of the corpus amylaceum (polyglucosan body). *Pathol. Oncol. Res. 7*, 145–150. https://doi.org/10.1053.paor.2001.0269

[10] Gentry, M.S., J.E. Dixon and C.A. Worby. **2009**. Lafora disease: insights into neurodegeneration from plant metabolism. *Trends Biochem. Sci. 34*, 628–639. https://doi.org/10.1016/j.tibs.2009.08.002

[11] Brewer, M.K., J.-L. Putaux, M. Sullivan, A. Rondon, A. Uittenbogaard and M.S. Gentry. **2020**. Polyglucosan body structure in Lafora disease. *Carbohydr. Polym. 240*, 116260. https://doi.org/10.1016/j.carbpol.2020.116260

[12] Potocki-Véronèse, G., J.-L. Putaux, D. Dupeyre, C. Albenne, M. Remaud-Simeon, P. Monsan, et al. **2005**. Amylose synthesized *in vitro* by amylosucrase: morphology, structure and properties. *Biomacromolecules 6*, 1000–1011. https://doi.org/10.1021/bm049326g

[13] Kajiura, H., H. Takata, T. Kuriki and S. Kitamura. **2010**. Structure and solution properties of enzymatically synthesized glycogen. *Carbohydr. Res. 345*, 817–824. https://doi.org/10.1016/j.carres.2010.01.013

[14] Ciric, J., A.J.J. Woortman, P. Gordiichuk, M.C.A. Stuart and K. Loos. **2013**. Physical properties and structure of enzymatically synthesized amylopectin analogs. *Starch/Stärke 65*, 1061–1068. https://doi.org/10.1002/star.201300063

[15] Putaux, J.-L., G. Potocki-Véronèse, M. Remaud-Simeon and A. Buléon. **2006**. Alpha-D-glucan-based dendritic nanoparticles prepared by *in vitro* enzymatic chain extension of glycogen. *Biomacromolecules 7*, 1720–1728. https://doi.org/10.1021/bm050988v

[16] Putaux, J.-L., S. Molina-Boisseau, T. Momaur and A. Dufresne. **2003**. Platelet nanocrystals resulting from the acid hydrolysis of waxy maize starch granules. *Biomacromolecules 4*, 1198–1202. https://doi.org/10.1021/bm0340422

[17] Helbert, W., H. Chanzy, V. Planchot, A. Buléon and P. Colonna. **1993**. Morphological and structural features of amylose spherocrystals of A-type. *Int. J. Biol. Macromol. 15*, 183–187. https://doi.org/10.1016/0141-8130(93)90021-D

[18] Hejazi, M., J. Fettke, O. Paris and M. Steup. **2009**. The two plastidial starch-related dikinases sequentially phosphorylate glucosyl residues at the surface of both the A- and B-type allomorphs of crystallized maltodextrins but the mode of action differs. *Plant Physiol. 150*, 962–976. https://doi.org/10.1104/pp.109.138750

[19] Montesanti, N., G. Véronèse, A. Buléon, P.C. Escalier, S. Kitamura and J.-L. Putaux. **2010**. A-type crystals from dilute solutions of short amylose chains. *Biomacromolecules 11*, 3049–3058. https://doi.org/10.1021/bm1008712

[20] Frost, K., D. Kaminski, G. Kirwan, E. Lascaris and R. Shanks. **2009**. Crystallinity and structure of starch using wide angle X-ray scattering. *Carbohydr. Polym. 78*, 543–548. https://doi.org/10.1016/j.carbpol.2009.05.018

[21] Zhu, F. **2017**. Atomic force microscopy of starch systems. *Crit. Rev. Food Sci. Nutr. 57*, 3127–3144. https://doi.org/10.1080/10408398.2015.1094650

[22] Stokes, D.J. **2008**. "Principles and Practice of Variable Pressure/Environmental Scanning Electron Microscopy (VP-ESEM)", John Wiley & Sons LtD, UK.

[23] Stabentheiner, E., A. Zankel and P. Pölt. **2010**. Environmental scanning electron microscopy (ESEM) – a versatile tool in studying plants. *Protoplasma 246*, 89–99. https://doi.org/10.1007/s00709-010-0155-3

[24] James, B. **2009**. Advances in "wet" electron microscopy techniques and their application to the study of food structure. *Trends Food Sci. Technol. 20*, 114–124. https://doi.org/10.1016/j.tifs.2009.01.057

[25] Watt, I.M. **1997**. "The Principles and Practice of Electron Microscopy", Cambridge University Press.

[26] Szczygieł, J., K. Dyrek, K. Kruczała, E. Bidzińska, Z. Brożek-Mucha, E. Wenda, et al. **2014**. Interactions of chromium ions with starch granules in an aqueous environment. *J. Phys. Chem. B 118*, 7100−7107. https://doi.org/0.1021/jp502028d

[27] Chauhan, K., V. Priya, P. Singh, G.S. Chauhan, S. Kumari and R.K. Singhal. **2015**. A green and highly efficient sulfur functionalization of starch. *RSC Adv. 5*, 51762. https://doi.org/10.1039/c5ra07332d

[28] Jane, J., Y. Kasemsuwan, S. Leas, H. Zobel and J.F. Robyt. **1994**. Anthology of starch granule morphology by scanning electron microscopy. *Starch/Stärke 46*, 121–129. https://doi.org/10.1002/star.19940460402

[29] Putaux, J.-L., D. Dupeyre, B. Pontoire, J. Davy, A. Buléon, C. d'Hulst, et al. **2010**. Amidothèque: an online database on the morphology, structure and composition of native starch granules. https://amidotheque.cermav.cnrs.fr

[30] Ao, Z. and J. Jane. **2007**. Characterization and modeling of the A- and B-granule starches of wheat, triticale, and barley. *Carbohydr. Polym. 67*, 46–55. https://doi.org/10.1016/j.carbpol.2006.04.013

[31] Wang, S., J. Yu, Q. Zhu, J. Yu and F. Jin. **2009**. Granular structure and allomorph position in C-type Chinese yam starch granule revealed by SEM, ^{13}C CP/MAS NMR and XRD. *Food Hydrocoll. 23*, 426–433. https://doi.org/10.1016/j.foodhyd.2008.02.012

[32] Kong, X., J. Bao and H. Corke. **2009**. Physical properties of *Amaranthus* starch. *Food Chem. 113*, 371–376. https://doi.org/10.1016/j.foodchem.2008.06.028

[33] Mahlberg, P.G. **1973**. Scanning electron microscopy of starch grains from latex of *Euphorbia terracina* and *E. tirucalli*. *Planta 110*, 77–80. https://doi.org/10.1007/BF00386925

[34] Seshagiri Rao, K. and M.N.V. Prasad. **1988**. Typology of latex starch grains of certain *Euphorbiaceae* and their possible significance in systematics. *Plant Syst. Evol. 160*, 189-193. https://doi.org/10.1007/BF00936046

[35] Chanzy, H., J.-L. Putaux, D. Dupeyre, R. Davies, M. Burghammer, S. Montanari, et al. **2006**. Morphological and structural aspects of the giant starch granules from *Phajus grandifolius*. *J. Struct. Biol. 154*, 100–110. https://doi.org/10.1016/j.jsb.2005.11.007

[36] Izumo, A., S. Fujiwara, T. Sakurai, S.G. Ball, Y. Ishii, H. Ono, et al. **2011**. Effects of granule-bound starch synthase I-defective mutation on the morphology and structure of pyrenoidal starch in *Chlamydomonas*. *Plant Sci. 180*, 238–245. https://doi.org/10.1016/j.plantsci.2010.08.014

[37] Lin, Q., M. Facon, J.-L. Putaux, J.R. Dinges, F. Wattebled, C. D'Hulst, et al. **2013**. Function of isoamylase-type starch debranching enzymes ISA1 and ISA2 in *Zea mays* leaf. *New Phytol. 200*, 1009–1021. https://doi.org/10.1111/nph.12446

[38] Vandromme, C., C. Spriet, D. Dauvillée, A. Courseaux, J.-L. Putaux, A. Wychowski, et al. **2019**. PII1: a protein involved in starch initiation that determines granule number and size in Arabidopsis chloroplast. New Phytol. 221: 356–370. https://doi.org/10.1111/nph.15356

[39] Baldwin, P.M., D.J. Gallant and S. Pérez. **2009**. Structural features of starch granules I. In "Starch: Chemistry and Technology (Third Edition)", J. BeMiller and R. Whistler eds, Chapter 5, pp 149–192.

[40] Blazek, J. and L. Copeland. **2010**. Amylolysis of wheat starches. II. Degradation patterns of native starch granules with varying functional properties. *J. Cereal Sci. 52*, 295–302. https://doi.org/10.1016/j.jcs.2010.06.011

[41] Hasjim, J., G. Cesbron Lavau, M.J. Gidley and R.G. Gilbert. **2010**. In vivo and in vitro starch digestion: are current in vitro techniques adequate? *Biomacromolecules 11*, 3600–3608. https://doi.org/10.1021/bm101053y

[42] Soares, C.A., F.H.G. Peroni-Okita, M.B. Cardoso, R. Shitakubo, F.M. Lajolo and B. R. Cordenunsi. **2011**. Plantain and banana starches: granule structural characteristics explain the differences in their starch degradation patterns. *J. Agric. Food Chem. 59*, 6672–6681. https://doi.org/10.1021/jf201590h

[43] Huang, J., N. Wei, H. Li, S. Liu and D. Yang. **2014**. Outer shell, inner blocklets, and granule architecture of potato starch. *Carbohydr. Polym. 103*, 355–358. https://doi.org/10.1016/j.carbpol.2013.12.064

[44] Dhital, S., V.M. Butardo Jr., S.A. Jobling and M.J. Gidley. **2015**. Rice starch granule amylolysis – Differentiating effects of particle size, morphology, thermal properties and crystalline polymorph. *Carbohydr. Polym. 115*, 305–316. http://dx.doi.org/10.1016/j.carbpol.2014.08.091

[45] Fanta, G.F., F.C. Felker and R.L. Shogren. **2002**. Formation of crystalline aggregates in slowly-cooled starch solutions prepared by steam jet cooking. *Carbohydr. Polym. 48*, 161–170. https://doi.org/10.1016/S0144-8617(01)00230-2

[46] Singh, J., C. Lelane, R.B. Stewart and H. Singh. **2010**. Formation of starch spherulites: Role of amylose content and thermal events. Food Chem. 121: 980–989. https://doi.org/10.1016/j.foodchem.2010.01.032

[47] Kiatponglarp, W., S. Rugmai, A. Rolland-Sabaté, A. Buléon and S. Tongta. **2016**. Spherulitic self-assembly of debranched starch from aqueous solution and its effect on enzyme digestibility. *Food Hydrocoll. 55*, 235–243. https://doi.org/10.1016/j.carbpol.2010.10.041

[48] Li, B.-Z., X.Q. Xian, Y. Wang, B. Adhikari and D. Chen. **2018**. Production of recrystallized starch microspheres using water-in-water emulsion and multiple recycling of polyethylene glycol solution. *LWT - Food Sci. Technol. 97*, 76–82. https://doi.org/10.1016/j.lwt.2018.06.034

[49] Fannon, J.E., R.J. Hauber and J.N. BeMiller. **1992**. Surface pores of starch granules. *Cereal Chem. 69*, 284–288.

[50] Dang, J.M.C. and L. Copeland. **2004**. Studies of the fracture surface of rice grains using environmental scanning electron microscopy. *J. Sci. Food Agric. 84*, 707–713. https://doi.org/10.1002/jsfa.1671

[51] Edwards, M.A., B.G. Osborne and R.J. Henri. **2008**. Effect of endosperm starch granule size distribution on milling yield in hard wheat. *J. Cereal Sci. 48*, 180–192. https://doi.org/10.1016/j.jcs.2007.09.001

[52] Barrera, G.N., G. Calderón-Domínguez, J. Chanona-Pérez, G.F. Gutiérrez-López, A.E. León and P.D. Ribotta. **2013**. Evaluation of the mechanical damage on wheat starch granules by SEM, ESEM, AFM and texture image analysis. *Carbohydr. Polym. 98*, 1449–1457. http://dx.doi.org/10.1016/j.carbpol.2013.07.056

[53] Tang, X., M. De Rooij and L. De Jong. **2007**. Volume change measurements of rice by environmental scanning electron microscopy and stereoscopy. *Scanning 29*, 197–205. https://doi.org/10.1002/sca.20064

[54] Fechner, P.M., S. Wartewig, A. Kiesow, A. Heilmann, P. Kleinebudde and R.H.H Neubert. **2005**. Influence of water on molecular and morphological structure of various starches and starch derivatives. *Starch/Stärke 57*, 605–615. https://doi.org/10.1002/star.200500410

[55] Aebi, U. and T.D. Pollard. **1987**. A glow discharge unit to render electron microscope grids and other surfaces hydrophilic. *J. Electron. Microsc. Tech 7*, 29–33. https://doi.org/10.1002/jemt.1060070104

[56] Harris, J.R. **1997**. "Negative Staining and Cryoelectron Microscopy: The Thin Film Techniques", RMS Microscopy Handbook, Oxford, BIOS Scientific Publishers.

[57] Husemann, E. and H. Ruska. **1940**. Versuche zur Sichtbarmachung voxi Glykogenmolekülen. *J. prakt. Chemie 156*, 1–10. https://doi.org/10.1002/prac.19401560101

[58] Hosogi, N., H. Nishioka and M. Nakakoshi. **2015**. Evaluation of lanthanide salts as alternative stains to uranyl acetate. *Microscopy 64*, 429–425. https://doi.org/10.1093/jmicro/dfv054

[59] Kuipers, J. and B.N.M. Giepmans. **2020**. Neodymium as an alternative contrast for uranium in electron microscopy. Histochem. *Cell Biol. 153*, 271–277. https://doi.org/10.1007/s00418-020-01846-0

[60] Drochmans, P. **1962**. Morphologie du glycogène: Etude au microscope électronique de colorations négatives du glycogène particulaire. *J. Ultrastruct. Res. 6*, 141–163.

[61] Sullivan, M.A., F. Vilaplana, R.A. Cave, D. Stapleton, A.A. Gray-Weale and R.G. Gilbert. **2010**. Nature of α and β particles in glycogen using molecular size distributions. Biomacromolecules 11: 1094–1100. https://doi.org/10.1021/bm100074p

[62] Sullivan, M.A., J. Li, C. Li, F. Vilaplana, D. Stapleton, A.A. Gray-Weale, et al. **2011**. Molecular structural differences between type-2-diabetic and healthy glycogen. *Biomacromolecules 12*, 1983–1986. https://doi.org/10.1021/bm2006054

[63] Hu, Z., B. Deng, X. Tan, H. Gane, C. Li, S.S. Nada, et al. **2018**. Diurnal changes of glycogen molecular structure in healthy and diabetic mice. *Carbohydr. Polym. 185*, 145–152. https://doi.org/10.1016/j.carbpol.2018.01.003

[64] Wanson, J.-C. and P. Drochmans. **1968**. Rabbit skeletal muscle glycogen. A morphological and biochemical study of glycogen β-particles isolated by the precipitation-centrifugation method. *J. Cell Biol. 38*, 130–150.

[65] Sullivan, M.A., M.J. O'Connor, F. Umana, E. Roura, K. Jack, D.I. Stapleton, et al. **2012**. Molecular insights into glycogen α-particle formation. *Biomacromolecules 13*, 3805−3813. https://doi.org/10.1021/bm3012727

[66] Powell, P.O., M.A. Sullivan, J.J. Sheehy, B.L. Schulz, F.J. Warren and R.G. Gilbert. **2015**. Acid hydrolysis and molecular density of phytoglycogen and liver glycogen helps understand the bonding in glycogen α (composite) particles. *PLoS ONE 10(3),* e0121337. https://doi.org/10.1371/journal.pone.0121337

[67] Hata, K., M. Hata, M. Hata and K. Matsuda. **1984**. A proposed model for glycogen particles. *J. Jpn. Soc. Starch Sci. 31*, 146–155. https://doi.org/10.5458/jag1972.31.146

[68] Matsuda, K. and Hata K. **1985**. The structure of glycogen particles. *J. Jpn. Soc. Starch Sci. 32*, 118–127.

[69] Putaux, J.-L., A. Buléon, R. Borsali and H. Chanzy. **1999**. Ultrastructural aspects of phytoglycogen from cryo-TEM and quasi-elastic light scattering data. *Int. J. Biol. Macromol. 26*, 145–150. https://doi.org/10.1016/S0141-8130(99)00076-8

[70] Huang, L. and Y. Yao. **2011**. Particulate structure of phytoglycogen nanoparticles probed using amyloglucosidase. *Carbohydr. Polym. 83*, 1665–1671. https://doi.org/10.1016/j.carbpol.2010.10.030

[71] Melendez-Hevia, E., T. G. Waddell and E. D. Shelton. **1993**. Optimization of molecular design in the evolution of metabolism: the glycogen molecule. *Biochem. J. 295*, 477–483. https://doi.org/10.1042/bj2950477

[72] Melendez, R., E; Melendez-Hevia and E. I. Canela. **1999**. The fractal structure of glycogen: A clever solution to optimize cell metabolism. *Biophys. J. 77*, 1327–1332. https://doi.org/10.1016/S0006-3495(99)76982-1

[73] Matsui, M., M. Kakut and A. Misaki. **1996**. Fine structural features of oyster glycogen: mode of multiple branching. *Carbohydr. Polym. 31*, 227–235. https://doi.org/10.1016/S0144-8617(96)00116-6

[74] Bezborodkina, N.N., A.Y. Chestnova, M.L. Vorobev and B.N. Kudryavtsev. **2018**. Spatial structure of glycogen molecules in cells. *Biochemistry (Moscow) 83*, 467–482. https://doi.org/10.1134/S0006297918050012

[75] Zhang, P., S. Nada, X. Tan, B. Deng, M.A. Sullivan and R.G. Gilbert. **2018**. Exploring glycogen biosynthesis through Monte Carlo simulation. *Int. J. Biol. Macromol. 116*, 264–271. https://doi.org/10.1016/j.ijbiomac.2018.05.027. **2020**. Erratum to "Exploring glycogen biosynthesis through Monte Carlo simulation". *Int. J. Biol. Macromol. 144*, 1043–1044. https://doi.org/10.1016/j.ijbiomac.2019.05.183

[76] Kajiura, H., H. Takata, T. Akiyama, R. Kakutani, T. Furuyashiki, I. Kojima, et al. **2011**. *In vitro* synthesis of glycogen: the structure, properties, and physiological function of enzymatically-synthesized glycogen. *Biologia 66*, 387–394. https://doi.org/10.2478/s11756-011-0053-y

[77] Roussel, X., C. Lancelon-Pin, A. Viksø-Nielsen, A. Rolland-Sabaté, F. Grimaud, G. Véronèse, et al. **2013**. Characterization of substrate and product specificity of the purified recombinant glycogen branching enzyme of *Rhodothermus obamensis*. *Biochim. Biophys. Acta - Gen. Subj. 1830*, 2167–2177. https://doi.org/10.1016/j.bbagen.2012.09.022

[78] Grimaud, F., X. Roussel, C. Lancelon-Pin, S. Laguerre, A. Viksø-Nielsen, A. Rolland-Sabaté, et al. **2013**. In vitro synthesis of hyperbranched α-glucans using a biomimetic enzymatic toolbox. *Biomacromolecules 14*, 438–447. https://doi.org/10.1021/bm301676c

[79] Deschamps, P., C. Colleoni, Y. Nakamura, E. Suzuki, J.-L. Putaux, A. Buléon, et al. **2008**. Metabolic symbiosis and the birth of the plant kingdom. *Mol. Biol. Evol. 25*, 536–548. https://doi.org/10.1093/molbev/msm280

[80] Shimonaga, T., M. Konishi, Y. Oyama, S. Fujiwara, A. Satoh, N. Fujita, et al. **2008**. Variation in storage α-polyglucans of the *Porphyridiales (Rhodophyta)*. *Plant Cell Physiol. 49*, 103–116. https://doi.org/10.1007/s10126-006-6104-7

[81] Harris, J.R., M. Adrian and F. Petry. **2004**. Amylopectin: a major component of the residual body in *Cryptosporidium parvum* oocysts. *Parasitology 128*, 269–282. https://doi.org/10.1017/S003118200300458X

[82] Robin, J.-P., C. Mercier, R. Charbonnière and A. Guilbot. **1974**. Lintnerized starches. Gel filtration and enzymatic studies of insoluble residues from prolonged acid treatment of potato starch. *Cereal Chem. 51*, 389–406.

[83] Yamaguchi, M., K. Kainuma and D. French. **1979**. Electron microscopic observations of waxy maize starch. *J. Ultrastruct. Res. 69*, 249–261. https://doi.org/10.1016/S0022-5320(79)90114-X

[84] Angellier-Coussy, H., J.-L. Putaux, S. Molina-Boisseau, A. Dufresne, E. Bertoft and S. Pérez. **2009**. The molecular structure of waxy maize starch nanocrystals. *Carbohydr. Res. 344*, 1558–1566. https://doi.org/10.1016/j.carres.2009.04.002

[85] Wikman, J., A. Blennow, A. Buléon, J.-L. Putaux, S. Pérez, K. Seetharaman, et al. **2014**. Influence of amylopectin structure and degree of phosphorylation on the molecular composition of potato starch lintners. *Biopolymers 101*, 257–271. https://doi.org/10.1002/bip.22344

[86] Goldstein, A., G. Annor, J.-L. Putaux, K.H. Hebelstrup, A. Blennow and E. Bertoft. Impact of full range of amylose contents on the architecture of starch granules. **2016**. *Int. J. Biol. Macromol. 89*, 305–318. https://doi.org/10.1016/j.ijbiomac.2016.04.053

[87] Dubochet, J., M. Adrian, J. J. Chang, J.-C. Homo, J. Lepault, A.W. McDowall and P. Schultz. **1988.** Cryo-electron microscopy of vitrified specimens. *Q. Rev. Biophys. 21*, 129–228. https://doi.org/10.1007/978-3-642-72815-0_5

[89] Martinez-Garcia, M., M.C.A. Stuart and M.J.E.C. van der Maarel. **2016**. Characterization of the highly branched glycogen from the thermoacidophilic red microalga *Galdieria sulphuraria* and comparison with other glycogens. *Int. J. Biol. Macromol. 89*, 12–18. https://doi.org/10.1016/j.ijbiomac.2016.04.051

[90] Glauert, A.M. **1975**. "Fixation, Dehydration and Embedding of Biological Specimens", North-Holland/American, Elsevier.

[91] Reid, N. **1975**. "Practical Methods in Electron Microscopy: Ultramicrotomy", North-Holland/American: Elsevier.

[92] Ramanazov, Z., M. Rawat, M.C. Henk, CB. Mason, S.W. Matthews and J.V. Moroney. **1994**. The induction of the CO_2-concentrating mechanism is correlated with the formation of the starch sheath around the pyrenoid of *Chlamydomonas reinhardtii*. *Planta 195*, 210–216. https://doi.org/10.1007/BF00199681

[93] Roldán, I., F. Wattebled, M.M. Lucas, D. Delvallé , V. Planchot, S. Jiménez, et al. **2007**. The phenotype of soluble starch synthase IV defective mutants of *Arabidopsis thaliana* suggests a novel function of elongation enzymes in the control of starch granule formation. *Plant J. 49*, 492–504. https://doi.org/10.1111/j.1365-313X.2006.02968.x

[94] Eicke, S., D. Seung, B. Egli, E.A. Devers and S. Streb. **2017**. Increasing the carbohydrate storage capacity of plants by engineering a glycogen-like polymer pool in the cytosol. *Metabolic Eng. 40*, 23–32. http://dx.doi.org/10.1016/j.ymben.2017.02.008

[95] Seung, D., T.B. Schreier, L. Bürgy, S. Eicke and S.C. Zeeman. **2018**. Two plastidial coiled-coil proteins are essential for normal starch granule initiation in Arabidopsis. *Plant Cell 30*, 1523–1542. https://doi.org/10.1105/tpc.18.00219

[96] Revel, J.-P., L. Napolitano, D.W. Fawcett. **1960**. Identification of glycogen in electron micrographs of thin tissue sections. *J. Biophys. Biochem Cytology 8*, 575–859. https://doi.org/10.1083/jcb.8.3.575

[97] Ryman, B.E. **1974**. The glycogen storage diseases. *J. Clin. Pathol. Suppl. (R. Coll. Pathol.) 8*, 106–121.

[98] Riemersma, J.C., E.J.J. Alsbach and W.C. De Bruijn. **1984**. Chemical aspects of glycogen contrast-staining by potassium osmate. *Histochem. J. 16*, 123–136. https://doi.org/10.1007/BF01003544

[99] De Bruijn, W.C. **1973**. Glycogen, its chemistry and morphologic appearance in the electron microscope. I. A modified OsO4 fixative which selectively contrasts glycogen. *J. Ultrastruct. Res. 42*, 29–50. https://doi.org/10.1016/S0022-5320(73)80004-8

[100] Gallant, D. and A. Guilbot. **1969**. Etude de l'ultrastructure du grain d'amidon à l'aide de nouvelles méthodes de préparation en microscopie électronique. *Die Stärke 6*, 156–163. https://doi.org/10.1002/star.19690210605

[101] Thiéry, J.-P. **1967**. Mise en évidence des polysaccharides sur coupes fines en microscopie électronique. *J. Microscopie 6*, 987–1018.

[102] Gérard, C., P. Colonna, B. Bouchet, D. J. Gallant and V. Planchot. **2001**. A multi-stages biosynthetic pathway in starch granules revealed by the ultrastructure of maize mutant starches. *J. Cereal Sci. 34*, 61–71. https://doi.org/10.1006/jcrs.2001.0375

[103] Cenci, H., M. Chabi, M. Ducatez, C. Tirtiaux, J. Nirmal-Raj, Y. Utsumi, et al. **2013**. Convergent evolution of polysaccharide debranching defines a common mechanism for starch accumulation in cyanobacteria and plants. *Plant Cell 25*, 3961–3975. https://doi.org/10.1105/tpc.113.118174

[104] Kadouche, D., M. Ducatez, U. Cenci, C. Tirtiaux, E. Suzuki, Y. Nakamura, et al. **2016**. Characterization of function of the GlgA2 glycogen/starch synthase in *Cyanobacterium* sp. Clg1 highlights convergent evolution of glycogen metabolism into starch granule aggregation. *Plant Physiol. 171*, 1879–1892. https://doi.org/10.1104/pp.16.00049

[105] Boyer, L., X. Roussel, A. Courseaux, O. Mvundza Ndjindji, C. Lancelon-Pin, J.-L. Putaux, et al. **2016**. Expression of *Escherichia coli* glycogen branching enzyme in an Arabidopsis mutant devoid of endogenous starch branching enzymes induces the synthesis of starch-like polyglucans. *Plant, Cell Environ. 39*, 1432–1447. https://doi.org/10.1111/pce.12702

[106] Gallant, D.J. and A. Guilbot. **1971**. Artefacts au cours de la préparation de coupes de grains d'amidon. Etude par microscopie photonique et électronique. Die Stärke 23: 244–250. https://doi.org/10.1002/star.19710230707

[107] Helbert, W. and H. Chanzy. **1996**. The ultrastructure of starch from ultrathin sectioning in melamine resin. *Starch/Stärke 48*, 185–188. https://doi.org/10.1002/star.19960480507

[108] Peroni-Okita, F.H.G., P. Gunning, A. Kirby, R.A. Simao, C.A. Soares and B.R. Cordenunsi. **2015**. Visualization of internal structure of banana starch granule through AFM. Carbohydr. Polym. 128, 32-40. https://doi.org/10.1016/j.carbpol.2015.04.019

[109] Tsukamoto, K., T. Ohtani, S. Sugiyama. **2012**. Effect of sectioning and water on resin-embedded sections of corn starch granules to analyze inner structure. *Carbohydr. Polym. 89*, 1138–1149. https://doi.org/10.1016/j.carbpol.2012.03.087

[110] Chanzy, H., R. Vuong and J.-C. Jésior. **1990**. An electron diffraction study on whole granules of lintnerized potato starch. *Starch/Staerke 42*, 377–379. https://doi.org/10.1002/star.19900421003

[111] Oostergetel, G.T. and E.F.J. van Bruggen. **1993**. The crystalline domains in potato starch granules are arranged in a helical fashion. *Carbohydr. Polym. 21*, 7–12. https://doi.org/10.1016/0144-8617(93)90110-P

[112] Nudelman, F., G. de With and N.A.J.M. Sommerdijk. **2011**. Cryo-electron tomography: 3-dimensional imaging of soft matter. *Soft Matter 7*, 17−24. https://doi.org/10.1039/c0sm00441c

[113] Fridman, K., A. Mader, M. Zwerger, N. Elia, O. Medalia. **2012**. Advances in tomography: probing the molecular architecture of cells. *Nat. Rev. Mol. Cell. Biol. 13*, 736–742. https://doi.org/10.1038/nrm3453

[114] Engel, B.D., M. Schaffer, L.K. Cuellar, E. Villa, J.M. Plitzko and W. Baumeister. **2015**. Native architecture of the *Chlamydomonas* chloroplast revealed by in situ cryo-electron tomography. *eLife 4*, e04889. https://doi.org/10.7554/eLife.04889